

40 GHz mode-locked semiconductor lasers: theory, simulations and experiment

UWE BANDELOW^{1,*}, MINDAUGAS RADZIUNAS¹, ANDREI VLADIMIROV¹, BERND HÜTTL² AND RONALD KAISER²

¹Weierstraß-Institut für Angewandte Analysis und Stochastik (WIAS), Mohrenstrasse 39, D-10117 Berlin, Germany

²Fraunhofer-Institut für Nachrichtentechnik, Heinrich-Hertz-Institut (HHI), Einsteinufer 37, D-10587 Berlin, Germany

(*author for correspondence: E-mail: bandelow@wias-berlin.de)

Received 7 June 2005; accepted 26 January 2006

Abstract. We study both theoretically and experimentally typical operation regimes of 40 GHz monolithic mode-locked lasers. The underlying Traveling Wave Equation model reveals quantitative agreement for characteristics of the fundamental mode-locking as pulse width and repetition frequency tuning, as well as qualitative agreement with the experiments for other dynamic regimes. Especially the appearance of stable harmonic mode-locking at 80 GHz has been predicted theoretically and confirmed by measurements. Furthermore, we derive and apply a simplified Delay-Differential-Equation model which guides us to a qualitative analysis of bifurcations responsible for the appearance and the breakup of different mode-locking regimes. Higher harmonics of mode-locking are predicted by this model as well.

Key words: delay-differential equations, harmonic mode-locking, mode-locking, traveling wave equations

1. Introduction

Mode-locked semiconductor lasers attract considerable interest since many years, for their high speed potential as well as the possible generation of intense pulses. In this paper, we study theoretically and experimentally different operation regimes of a monolithic mode-locked SIPBH¹ semiconductor multisection distributed Bragg reflector (DBR) laser suitable for optical data transmission at rates of 40 GHz and higher. The laser shown in Fig. 1 consists of four sections: a reversely biased saturable absorber section S_A , a forward biased gain section S_G , a passive phase tuning section S_P , and a passive DBR section S_R . Details of the laser architecture have been already described elsewhere (Kaiser *et al.* 2003).

The application of mode-locked lasers in high speed optical communication systems, e.g. in time division multiplexing systems at bit rates up to 160 Gb/s, implies that several important requirements on pulse quality have to be met. These requirements are still fundamental challenges in mode-locked semiconductor lasers, especially if very short optical pulses and low amplitude noise have to be achieved simultaneously at high repetition rates. In this

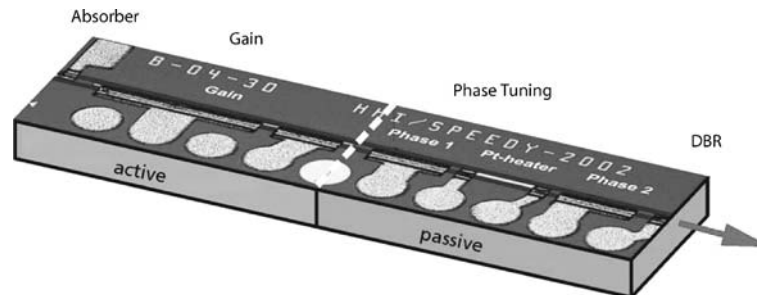


Fig. 1. Multisection DBR laser as fabricated at HHI Berlin. For parameters see Table 1.

contribution, comprehensive simulations and theoretical considerations are performed on monolithically integrated 40 GHz mode-locked multi-quantum well lasers, first to demonstrate the validity of the models, and second to analyze and to understand the dynamic effects which can appear in the laser.

The paper is organized as follows. In Section 2, we present the general frame of our model, which is based on the Traveling Wave Equations (TWE), and specify the modeling of the individual sections of the device. Following that we present results obtained by numerical simulations with this TWE model. In Section 3, we compare such simulation results with experimental data. In particular, we identify typical parameter regions for mode-locking (ML) and perturbations of ML, which guide us to more complicated dynamics. Such scenarios will be discussed in more detail also in Section 3. The most surprising effect within this paper is the appearance of stable harmonic ML at 80 GHz repetition frequency, to which we dedicate the second part of Section 3. This harmonic ML was first predicted by our TWE model and appears without a special preparation in our device, both in simulations and experiments. To understand and to analyze this phenomenon in more detail we apply in Section 4 a delay-differential equation (DDE) model which approximates the TWE model for ML lasers (Vladimirov *et al.* 2004). This DDE model guides us to a qualitative understanding of the observed phenomena by revealing the generic bifurcation structure behind them. Most important in our context it demonstrates, that the harmonic ML is a generic feature for our devices. Moreover, the appearance of even higher harmonic ML at 120 GHz is also predicted by the DDE model as will be presented and discussed in Section 4.

2. Theory

In a mode-locked laser a spatio-temporal distribution of the electric field develops across the entire device and has to be properly accounted for. An adequate description is given by the traveling wave equations

$$\left(-\frac{i}{v_g} \frac{\partial}{\partial t} \mp i \frac{\partial}{\partial z} + \beta\right) E^\pm + \kappa E^\mp = F_{\text{sp}}^\pm \quad (1)$$

for the slowly varying amplitudes $E^+(z, t)$ and $E^-(z, t)$ of the forward and backward travelling waves, respectively. The boundary conditions are $E^-(L, t) = 0$ at the anti-reflection (AR) coated facet of the DBR section ($z = L$) and $E^+(0, t) = r_0 E^-(0, t)$ at the cleaved facet of the absorber section ($z = 0$). By proper normalization, $|E(z, t)|^2 = |E^+|^2 + |E^-|^2$ is a local photon density.² β describes the propagation properties of the fundamental transverse mode of the internal waveguide at the central frequency ω_0 . The counterpropagating waves are mutually coupled in the DBR section with the coupling strength κ . Except in this section, κ disappears. F_{sp}^\pm represent the spontaneous emission contributions introduced as the Langevin forces (see, e.g., Wünsche *et al.* 2003).

We use different models for the propagation factor β in different sections. In the passive phase tuning and DBR sections, it is a constant that is expressed via a linear nonresonant optical loss coefficient α as³

$$\beta(z) = -i \frac{\alpha}{2} \quad (z \in S_{P,R}). \quad (2)$$

In the gain and absorber sections, the propagation parameter is defined by

$$\beta = -i \frac{\alpha}{2} + \frac{g}{2} \left(\frac{i}{1 + \varepsilon \Gamma |E|^2} + \alpha_H \right) - i \mathcal{D} \quad (z \in S_{G,A}). \quad (3)$$

Here, α_H is the linewidth enhancement factor, ε is the gain compression factor and Γ is the transverse optical confinement factor. The spectral gain maximum g is given by the linear model

$$g = g(n) = g' \Gamma (n - n_{\text{tr}}) \quad (4)$$

with the gain slope g' and the transparency carrier density n_{tr} . The gain dispersion is taken into account by introducing into Equation (3) a linear operator \mathcal{D} defined by

$$\mathcal{D} E^\pm \stackrel{\text{def}}{=} \frac{\bar{g}}{2} (E^\pm - p^\pm), \quad (5)$$

where the polarization p^\pm obeys the linear oscillator equation corresponding to Lorentzian gain dispersion (Bandelow *et al.* 2001; Avrutin *et al.* 2005)

$$-i \partial_t p^\pm = -i \bar{\gamma} (E^\pm - p^\pm) + \bar{\omega} p^\pm. \quad (6)$$

Table 1. Simulation Parameters

Qty.	Absorber	Gain	meaning
l	40	372	Length of section (μm)
σ	0.0624	0.0624	Area of AZ (μm^2)
Γ	0.074	0.074	Transverse confinement factor
g'	400	43.3	Differential gain (10^{-21}m^2)
n_{tr}	0.2 ... 2.2	0.9	Transparency concentration ($10^{24}/\text{m}^3$)
ε	40	20	Nonlinear gain compression (10^{-24}m^3)
C	0	1.3	Auger recombination ($10^{-41} \text{m}^6/\text{s}$)
B	0	1	Bimolecular recombination ($10^{-16} \text{m}^3/\text{s}$)
τ	0.015	5	carrier lifetime (ns)
α_H	-1	-4.5	Linewidth enhancement factor
α	15	15	Waveguide loss (1/cm)
I	0	0 ... 150	Injection current (mA)
R_s	5	5	Series resistance (Ω)
U'_F	1.2	1.2	Fermi voltage drop (10^{-25}Vm^3)
\bar{g}	100	100	Amplitude of gain dispersion (1/cm)
$2\bar{\gamma}$	70	70	Full width at half maximum (rad/ps)

The phase section has $l = 636 \mu\text{m}$, $\alpha = 3.5/\text{cm}$, and $\bar{g} = 0$. The DBR section has $l = 48 \mu\text{m}$, $\alpha = 3.5/\text{cm}$, $\kappa = 165/\text{cm}$, $\bar{g} = 100/\text{cm}$, and $2\bar{\gamma} = 70 \text{ rad/ps}$. Throughout the whole structure the group index $c/v_g = 3.6$ and the relative center frequency of the Lorentzian gain spectrum is $\bar{\omega} = 0$. The center wavelength $\lambda_0 = \frac{2\pi c}{\omega_0} = 1.55 \mu\text{m}$ is determined by the Bragg reflector. The reflection coefficient at the absorber facet is $r_0 = -\sqrt{0.3}$.

Height, width, and peak position relative to ω_0 of the Lorentzian are determined by the parameters \bar{g} , $2\bar{\gamma}$, and $\bar{\omega}$, respectively.

Strictly speaking, the parameters entering the propagation factor β in the saturable absorber section can depend on the voltage applied to this section. However, we will assume that all these parameters, except the transparency density n_{tr} , are fixed (see Table 1). The unsaturated absorption in the absorber section is then proportional to n_{tr} and given by Equation (4) with $n = 0$.

The evolution of the carrier densities in the absorber and in the gain section is described by the rate equation

$$\partial_t n = J - R(n) - v_g \Re e \left[E^* \left(\frac{g}{1 + \varepsilon \Gamma |E|^2} + 2D \right) E \right], \quad (7)$$

where $R(n) = n/\tau + Bn^2 + Cn^3$ corresponds to the usual polynomial recombination law. In the present study, we take into account longitudinal distribution of the carriers, by allowing the carrier densities to vary also with z . A quantitative description of this spatial hole burning requires to take into account the current self-distribution: the injection current density becomes also inhomogeneous in order to ensure a constant voltage along the electrical contact (Bandelow *et al.* 1992). For this purpose, we use the model

$$J(z, t) \Big|_{z \in S_j} = \frac{I_j}{e\sigma_j l_j} - \frac{U'_F}{e\sigma_j l_j R_s} (n(z, t) - \bar{n}_j(t)), \quad j = G, A \quad (8)$$

for the injection rate of Equation (7). Here and below, the subscript j attributes laser parameters to different laser sections S_j . The first term on the right-hand side of Equation (8) determines the average injection rate by the constant injection current I and the active volume σl of the section. The second term is the current self-distribution contribution linearized with respect to the deviation of the density from its spatial mean value $\bar{n}(t)$ beneath a given electrical contact. The derivative of the Fermi level separation U'_F and the series resistivity R_s are treated as constant parameters.

Results of numerical simulations obtained with the help of the TWE model described above and their comparison with the experimental data are presented in the next section. The parameter values used in the calculations were either measured directly, or determined by comparing the numerical simulations and the experimental data on mode-locked and other types of monolithic semiconductor lasers. The parameters are collected in Table 1, any deviations will be noted in the text.

3. Simulations

The TWE model has been studied with the help of the software `LDSL-tool`, which was developed for the simulation and analysis of the (L)ongitudinal (D)ynamics in multisection (S)emiconductor (L)asers (Wünsche *et al.* 2003; Radziunas *et al.* 2005). Using `LDSL-tool` we have systematically scanned the control parameter plane, displayed in Fig. 3, to detect the different types of solutions and to further analyze them. To identify ML regimes we have used the following engineering approach. We have estimated the signal-to-noise ratio (snr) for each non-stationary solution by comparing in the radio-frequency (rf)-spectrum the heights of the main spectral peak close to 40 GHz to those of most pronounced spectral peaks at low frequencies. A mode-locked state is then identified by $\text{snr} > 25$ dB (see Fig. 2(a)). Obviously, the abscissa position of the main spectral peak is giving the frequency indicated in Fig. 3.

For ML (or close-to ML) operation we have determined the mean period of the pulse-train and performed a sampling with this period. As it was discussed in Wünsche *et al.* (2003), such a choice of the sampling period gives a proper representation of the pulse time jitter. In the present work, the resulting eye diagrams have been used for estimation of pulse width, amplitude, and time jitter of the pulse sequence (see Fig. 2(b)).

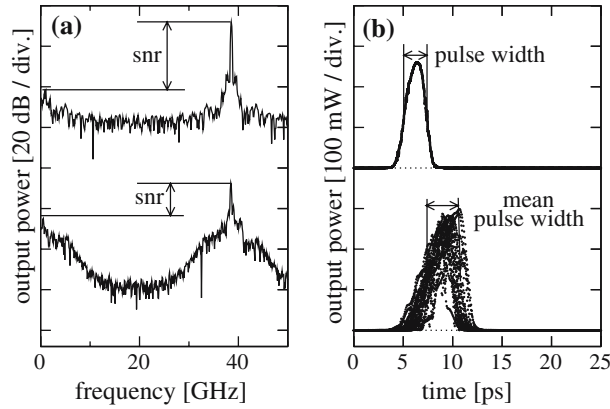


Fig. 2. Identification of mode-locking from radio-frequency spectra (a) and eye diagrams (b).

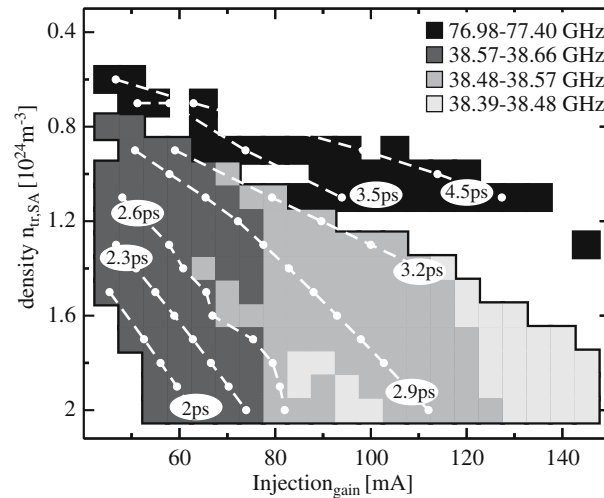


Fig. 3. Area of mode-locked operation in the plane $n_{tr,A}$ (proportional to the absorption) versus injection parameters calculated with `LDSE-tool`. Only pulsations with a signal-to-noise ratio > 25 dB are depicted. Different shadings and white lines show the main frequency of the output power and the mean width of mode locked pulses.

3.1. MODE-LOCKING AND PERTURBATIONS

First, we compare typical characteristics of passively mode-locked states obtained numerically with those measured experimentally. The domains of stable ML are shown by gray shaded areas in Figs. 3 and 4. The scale of transparency density n_{tr} (proportional to unsaturated absorption) in Fig. 3 is in agreement with experimentally estimated dependence of unsaturated absorption on the reverse voltage shown in Fig. 4. One can see that the numerically calculated pulse width and repetition frequency, which

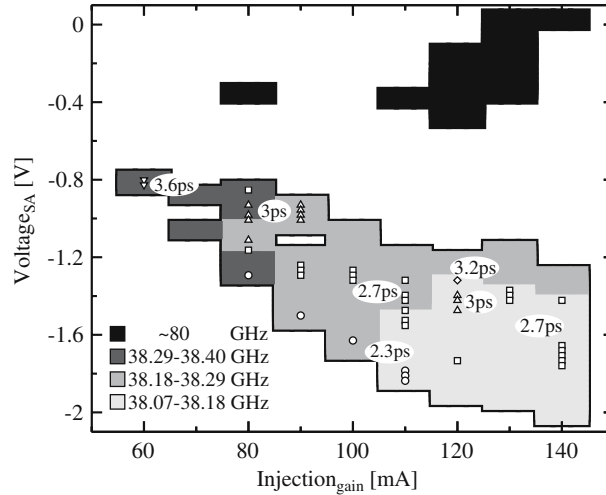


Fig. 4. Measured area of mode-locked operation in the plane absorber voltage versus injection current. Only pulsations with a $\text{snr} > 30$ dB are depicted. Different shadings show the main frequency of the output power. The mean width of mode locked pulses is indicated explicitly.

are indicated in Fig. 3, are in quite good agreement with the experimental data presented in Fig. 4. The pulse width decreases from 3.2 ps at the upper border of the ML-area to 2 ps at the lower edge of the ML-area with increasing absorber voltage. The pulse repetition frequency decreases monotonically from the upper left corner to the lower right corner of the ML-area by an amount of about 200 MHz in both figures.

At the borders of these gray shaded areas ML breaks and other dynamical regimes appear. Let us study such a transition between different operation regimes. For this we will walk along the diagonal from the lower left corner towards the upper right corner in Fig. 3.

Below the ML-area, near the lasing threshold, the well known low frequency Q-switching instability dominates and prevails the ML. This instability results in the pulse trains shown in Fig. 5(d)). When approaching the lower border of the ML area the Q-switching frequency of pulse packages monotonously increases up to approximately 4 GHz. Then a sharp transition to regular ML pulsations with approximately 40 GHz pulse repetition frequency occurs (Fig. 5(c)).

Close to the lower border of the ML area the resulting passive ML (Fig. 5(c)) is almost perfect even in the presence of spontaneous emission F_{sp} . When stepping further into the ML area and approaching the upper border of this region, a supermodulation of ML pulsations with a certain frequency below 2 GHz can be observed (see Fig. 5(b)). As long as our criterion $\text{snr} > 25$ dB is satisfied, we identify this regime as ML, although, it

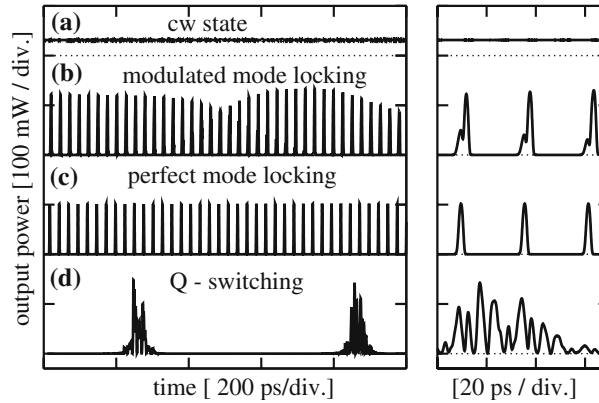


Fig. 5. Time traces of different operating regimes. Left: over a period of 1 ns, right: enlarged over a period of 50 ps. Parameters $n_{tr,A}$ ($10^{24}/m^3$) and I_G (mA) are 1 and 152 in. (a), 1.6 and 83 in. (b), 1.8 and 60 in. (c), 2 and 37 in. (d), respectively.

is imperfect ML. A closer inspection of this imperfect ML regime (right part of Fig. 5(b)) reveals the existence of a small satellite pulse accompanying the main pulse. The two pulses slowly modulate each other by changing their relative intensities. This process results in the strange envelope shown in Fig. 5(b)).

The appearance of the satellite pulse can be qualitatively explained by the existence of positive net gain at the leading edge of the main pulse. As a prerequisite, a pulse can only build up if there is a positive net gain per round trip. The classical ML mechanism assumes that the window of positive net gain is opened with the arrival of a pulse and is closed with its departure, so that at small pulse powers the net gain is always negative (New 1974). However, since the relaxation time of the gain section is much longer than that of the absorber section, at higher gain levels the situation is possible when the net gain becomes positive before the arrival of a pulse in the course of gain and loss relaxation process. For such pulses demonstrating positive net gain at their leading edge, any perturbation of the low intensity background near this edge will be amplified. Further evolution of these amplified perturbations sensitively depends on the net gain dynamics and their group velocity. If the group velocity of the perturbations is smaller than that of the pulses, they are absorbed by the pulse, which can preserve its stability in this case. However, at higher gains this mechanism becomes insufficient to stabilize the pulse train and it becomes unstable with the appearance of a satellite pulse, as it is illustrated by Fig. 5(b).

At the upper border of the ML-region our criterion $snr > 25$ dB is violated. Here, the supermodulation of the ML-pulses becomes very strong,

which results in noisy eye diagrams as presented in Fig. 2(c). When operating further apart from the 40 GHz ML area, we can find harmonic ML regimes discussed in the next subsection and, finally, reach a continuous-wave (CW) state, shown in Fig. 5(a).

3.2. HARMONIC MODE-LOCKING

The black shaded region in Fig. 3 indicates ML regimes with two pulses emitted from the laser within a single cavity round trip time (see upper diagrams of Fig. 6). Like in the examples given before, the quality of the ML solution has been determined by the inspection of rf spectra. The main frequency peak in the present case is close 80 GHz as shown in the middle diagrams of Fig. 6. We have evaluated the suppression snr of the corresponding low-frequency components, which had to be again > 25 dB. Left and right diagrams in Fig. 6 show two possible types of regular pulsations with a dominant 80 GHz component in the rf spectrum. In Fig. 6(a)–(c), we show 80 GHz harmonic ML, i.e. two identical pulses are emitted from the laser at each cavity round trip time. The 40 GHz component in the rf spectrum as well as each second mode in the optical spectrum is well suppressed. The latter can be visualized only by the activation of the spontaneous emission noise term F_{sp} in the model equations. In this situation the two pulses keep the maximum distance in the cavity and counter-propagate through it. Such behavior is characterized by completely correlated output pulses at the two end facets, with a repetition frequency of 80 GHz. Since this frequency is twice higher than that of the fundamental ML regime, we call the regime shown in Fig. 6(a)–(c) *harmonic ML*. The surprising thing is, that there is no specific geometrical construction as, e.g. a ring resonator or a colliding pulse scheme which would support this type of ML: the pulses meet simply somewhere in the phase tuning section without gaining from that. The harmonic ML appears to be self starting and is stable over a finite range of parameters.

Another type of stable periodic pulses with a frequency of 80 GHz dominating in rf-spectrum is illustrated by Fig. 6(d)–(f). However, now two subsequent pulses are different and both of them belong to the same single period which is equal to the cavity round trip time. This is the reason, why a 40 GHz component is well pronounced too in the rf spectra shown in Fig. 6(e). The optical spectrum of a corresponding output is similar to that of the fundamental ML regime, except that one single mode is strongly suppressed in the middle of the spectrum (see Fig. 6(f)). Such kind of pulsations could appear, for example, after period doubling of the 80 GHz ML regime. According to the data presented in Fig. 3 both the regimes

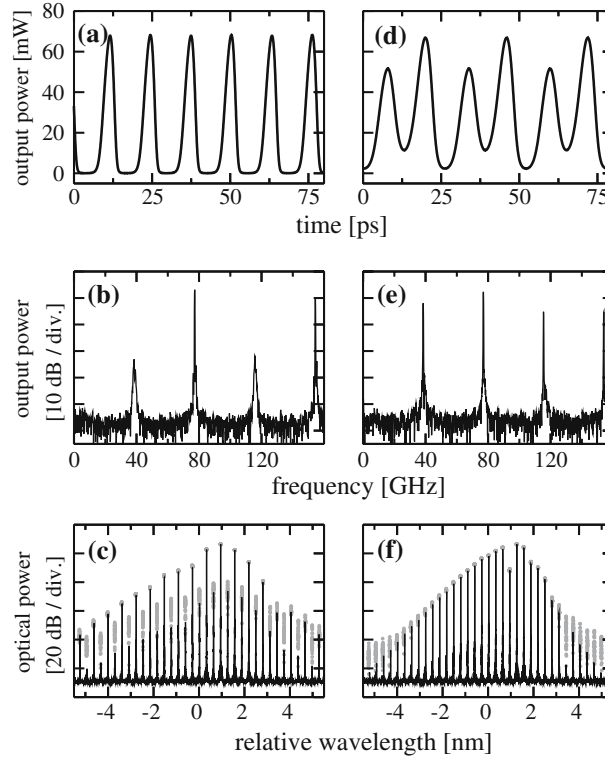


Fig. 6. Regular double pulse output within a single field round trip time. (a,d): time traces. (b,e): rf spectra. (c,f): optical spectra (lines), and instantaneously changing modal power versus modal wavelength computed by mode expansion technique (Radziunas *et al.* 2005) (grey bullets). $n_{tr,A} = 10^{24}/\text{m}^3$, $I_G = 100 \text{ mA}$ ((a)–(c)), and $I_G = 139 \text{ mA}$ ((d)–(f)).

presented in Fig. 6 are characterized by the pulse width larger than that of the fundamental regime with 40 GHz repetition rate.

So far, this was our first observation from numerical experiments with the TWE model. After this prediction this phenomenon of harmonic ML has been measured with autocorrelation techniques. The measured autocorrelation trace is depicted in the lower Fig. 7 and displays a periodic signal with a repetition frequency of 80 GHz, which corresponds to our prediction.

Even more, the harmonic ML has been measured in the same region of parameters as predicted by the theory, cf. the black areas in Fig. 3 and in Fig. 4. This harmonic ML regime could be applicable wherever high repetition frequencies or a switching between a basic frequency and its overtone in one device are desired. In the remainder, we want to discuss and apply further tools for a more qualitative analysis of the dynamical scenaria.

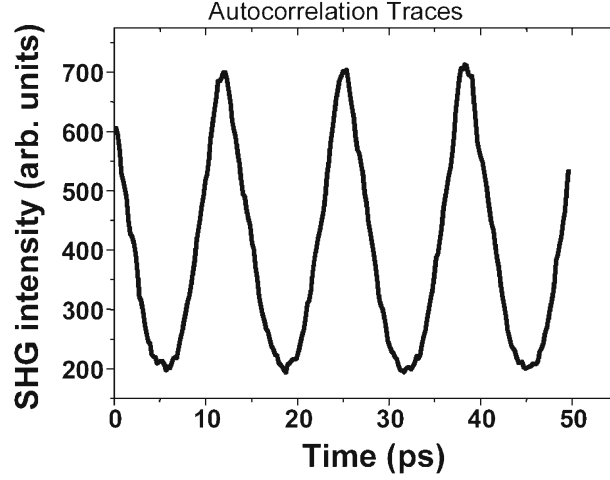


Fig. 7. Measured autocorrelation trace which indicates 80 GHz mode-locking.

4. Delay-differential equation model

In order to get qualitative understanding of bifurcation scenarios responsible for the appearance of harmonic ML and other dynamical regimes described above we use the DDE model proposed in Vladimirov *et al.* (2004). This model can be much easier analyzed numerically than the TWE model. In addition it allows for analytical studies in the limit of a slow saturable absorber, when the pulse duration is much shorter than the absorber relaxation time. The DDE model neglects Auger and bimolecular recombination as well as nonlinear gain compression and spatial hole burning. The profile of the spectral filtering element is assumed to be Lorentzian. In the case of ring cavity geometry the equations governing the time evolution of the electric field envelope $A(t)$ at the entrance of the saturable absorber section, cumulative saturable loss $Q(t) \propto \int_{S_A} n(z, t - z/v) dz$ and saturable gain $G(t) \propto \int_{S_G} n(z, t - z/v) dz$, introduced by the corresponding sections, take the form

$$\gamma^{-1} \frac{dA}{dt} = -A + \sqrt{\kappa} \exp \left[\frac{1 - i\alpha_{H,G}}{2} G(t-T) - \frac{1 - i\alpha_{H,A}}{2} Q(t-T) + i\phi \right] A(t-T), \quad (9)$$

$$\frac{dQ}{dt} = q_0 - \frac{Q}{\tau_A} - s [1 - \exp(-Q)] |A|^2, \quad (10)$$

$$\frac{dG}{dt} = g_0 - \frac{G}{\tau_G} - \exp(-Q) [\exp(G) - 1] |A|^2. \quad (11)$$

Here t is the dimensionless time normalized to a certain reference time interval Δt (below we set $\Delta t = 10$ ps). The index $A(G)$ refers to the absorber (gain) section, respectively. The cold cavity round trip time $T = L/v_g$ is equal to the cavity length L divided by the group velocity v_g of light, q_0 and g_0 are cumulative unsaturated loss and gain parameters which can be driven by the absorber voltage and the injection current in the gain section, respectively. The parameter γ describes the linewidth of the spectral filtering section, \varkappa is the linear nonresonant attenuation factor per cavity round trip which takes into account the reflectivity r_0 of the absorber facet, nonresonant internal losses α in the semiconductor medium, and maximum reflectivity of the Bragg filter. The parameter $s = g'_A/g'_G$ is the ratio of the differential gain parameters of the absorber and gain sections, ϕ describes the detuning between central frequency of the spectral filtering element and closest cavity mode. An advantage of the DDE models (9)–(11) is that it can be easily simulated by means of standard codes developed for solving DDEs (Guglielmi and Hairer 2000). The results of such simulations can be interpreted in terms similar to those introduced in classical ML theories, e.g. the net gain parameter given by $G - Q + \ln \kappa$. We note that Equations (9)–(11) do not assume small gain and losses per cavity round trip and weak absorber saturation. Therefore, unlike the Haus master equation (Haus 2001) they are valid in the typical parameter range of semiconductor lasers.

In the limit $\gamma T \rightarrow \infty$, which corresponds to the slow saturable absorber approximation, Equations (9)–(11) can be analyzed analytically. In this case, we split ML solution into two stages. First of them (slow stage) corresponds to the time interval between the two subsequent pulses when the electric field amplitude is very small. This stage is described by linear ordinary differential equations for the variables G and Q . The second (fast) stage corresponds to the short time interval when the pulse amplitude is large. At this stage the linear terms in Equations (10) and (11) can be neglected. Solving the laser equations for the two stages analytically and gluing the solutions one obtains the map governing the transformation of the pulse energy, saturable gain, and saturable loss after a complete round trip in the cavity. We skip the details of these calculations, which are described in Rachinskii and Vladimirov (2004), and present only the results of the analytical study of this map (see Fig. 8). Here, the grey area shows the domain of Q-switched 40 GHz ML. The horizontally and vertically dashed cones indicate the background stability domains of the fundamental ML regime (40 GHz) and a regime with twice higher repetition rate (80 GHz). These domains are defined by the New's stability condition which implies that the net gain $G - Q + \ln \varkappa$ must be negative during the whole slow stage (New 1974). Physically the background stability condition

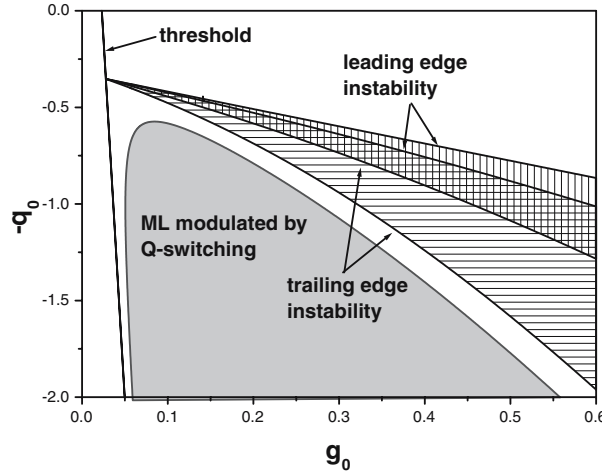


Fig. 8. Analytical stability analysis of ML solutions of the DDE model (9)–(11). Grey area indicates the instability domain of fundamental ML solution with respect to Q-switching instability. Horizontally and vertically dashed cones show the background stability domains of the 40 and 80 GHz ML. $\gamma = \infty$, $s = 25$, $\tau_A \Delta t = 13$ ps, $\tau_G \Delta t = 1$ ns, and $\kappa = 0.1$.

means that small perturbations of the low intensity background between ML pulses decay with time.

Fig. 8 provides a qualitative explanation for the numerical and experimental results shown in Figs. 3 and 4, respectively. Similarly to Fig. 8 the Q-switched ML regimes exist in the white areas below the ML stability domain in Figs. 3 and 4. In Fig. 8 the background stability domain of the 80 GHz ML regime is shifted to greater unsaturated gains g_0 with respect to that of the fundamental regime, which is in qualitative agreement with the experimental and numerical data from the TWE model. It also follows from this figure that the instability of the fundamental ML regime at high gain currents is connected to the presence of positive net gain at the pulse leading edge. Such kind of instability may lead to the appearance of a small additional pulse in front of the main pulse, similar to that shown in Fig. 5(b).

Now let us switch to a more detailed bifurcation analysis of Equations (9)–(11). The simplest solution of these equations corresponding to laser off is given by $A = 0$, $Q = q_0 \tau_A$, and $G = g_0 \tau_G$. Apart from this trivial solution CW solutions exist, which are characterized by nonzero time independent laser intensity above a certain threshold. The electric field envelope of a CW solution can be written in the form $A(t) = a \exp(i\gamma\omega t)$ where a is a time independent amplitude and ω is the frequency detuning normalized by the linewidth of the spectral filter. In the particular case, when the Henry factors of gain and absorber sections are equal, $\alpha_{HA} = \alpha_{HG} = \alpha_H$,

the frequencies of CW solutions are independent of the unsaturated gain parameter g_0 and are found from

$$\omega + \tan \chi = 0, \quad \chi = T\gamma\omega - \frac{\alpha_H}{2} \ln \left(\frac{1 + \omega^2}{\varkappa} \right) - \phi \quad (12)$$

with the additional condition $\cos \chi > 0$. The transcendental equation (12) has multiple solutions each corresponding to a certain CW solution which can be interpreted as “hot cavity mode”. The points where CW solutions bifurcate from the nonlasing solutions are defined by $g_0\tau_G = q_0\tau_A + \ln[(1 + \omega^2)/\varkappa]$. It follows from this relation that the CW solution with smallest absolute value of the frequency detuning $|\omega|$ bifurcates first with increasing g_0 . Therefore, the corresponding bifurcation point defines the so-called linear lasing threshold where the nonlasing solution loses its stability. All other CW solutions bifurcate from the nonlasing solution when it is already unstable. Therefore, such CW-solutions are unstable near the lasing threshold.

Hopf bifurcations of the CW solutions give rise to solutions with periodic laser intensity which (if stable) correspond to ML regimes. In Fig. 9, we present Hopf bifurcation curves of different CW solutions of Equations (9)–(11) calculated using the software package DDEBIFTOOL (Engelborghs *et al.* 2001). In this figure, the curves labeled QS correspond to the Hopf bifurcation that gives rise to a solution with pulsed laser intensity with the period approximately one order of magnitude greater than the cavity round trip time T . This bifurcation is related to the Q-switching instability. The Hopf bifurcation curves labeled n ($n = 1, 2, 3, 4, 5$) produce pulsed solutions with the periods close to T/n . These solutions correspond to ML regimes with different repetition rates. The bifurcation diagram shown in Fig. 9(b) corresponds to the CW solution with the frequency closest to the central frequency of the spectral filtering element. Therefore, unlike the curves shown in Figs. 9(a), 9(c), and 9(d) corresponding to bifurcations of unstable solutions, the curves in this diagram indicate the bifurcations of a stable cw solution. In this figure the bifurcation curve 1 indicates a Hopf bifurcation giving rise to a fundamental ML solution, while the bifurcations indicated two and three produce solutions with periodic laser intensity corresponding to harmonic ML regimes with the repetition rates close to 80 and 120 GHz, respectively. One can see that harmonic ML solutions appear at greater values of g_0 and q_0 than the fundamental ML solution. With the increase of the spectral filtering bandwidth γ the bifurcation thresholds of the harmonic ML solutions decrease.

Fig. 10 shows the transformation of dynamical regimes that occur with the increase of the unsaturated gain parameter g_0 . This diagram has been constructed using the following procedure. First, Equations (9)–(11) have

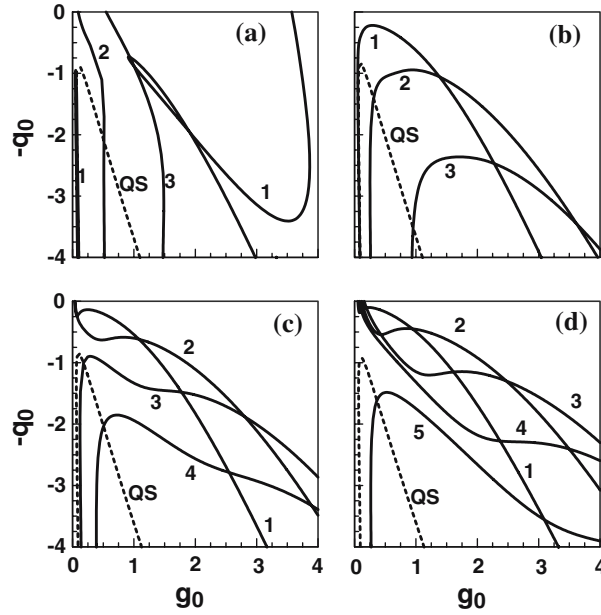


Fig. 9. Hopf bifurcation curves of the CW solutions. (a)–(d) correspond to $\omega = -3.58493$, -1.10106 , 1.34528 , and 3.75909 , respectively. $\gamma = 15$, $\alpha_{HG} = \alpha_{HA} = 3.5$, $\phi = 0$. The other parameters are the same as in Fig. 8.

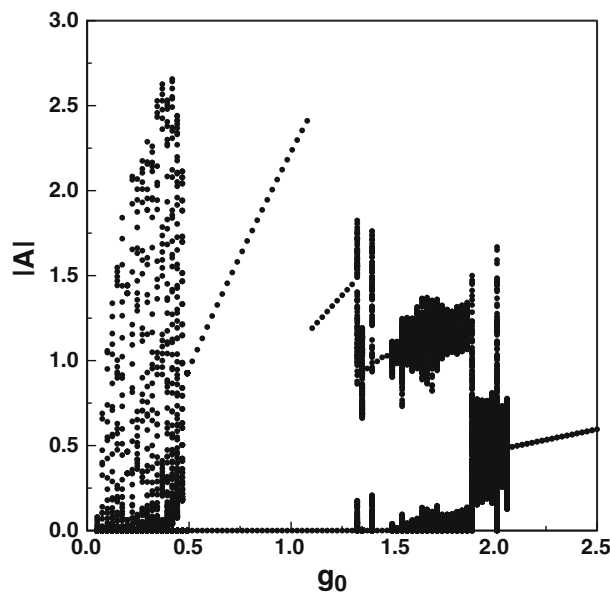


Fig. 10. Bifurcation diagram for Equations (9)–(11), $q_0 = 2$. The other parameters are the same as in Fig. 9.

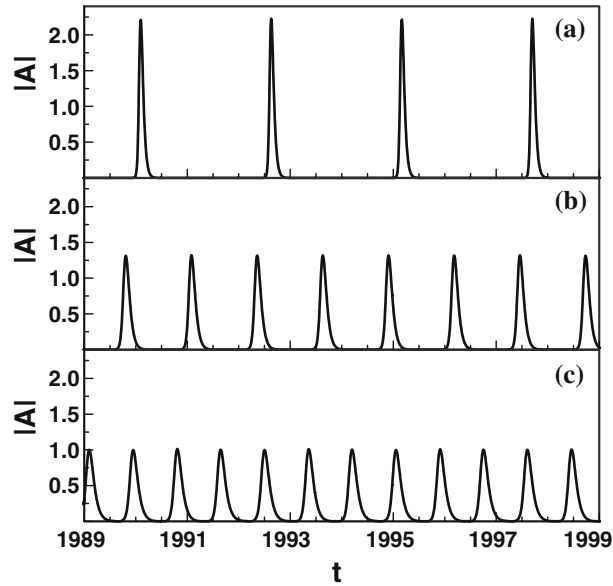


Fig. 11. Intensity timetraces of Equations (9)–(11) illustrating ML regimes with different repetition frequencies. $q_0 = 2$, (a) fundamental 40 GHz ML regime, $g_0 = 1.0$; (b) 80 GHz ML regime, $g_0 = 1.2$; (c) 120 GHz ML regime, $g_0 = 1.45$. Other parameters are the same as in Fig. 9.

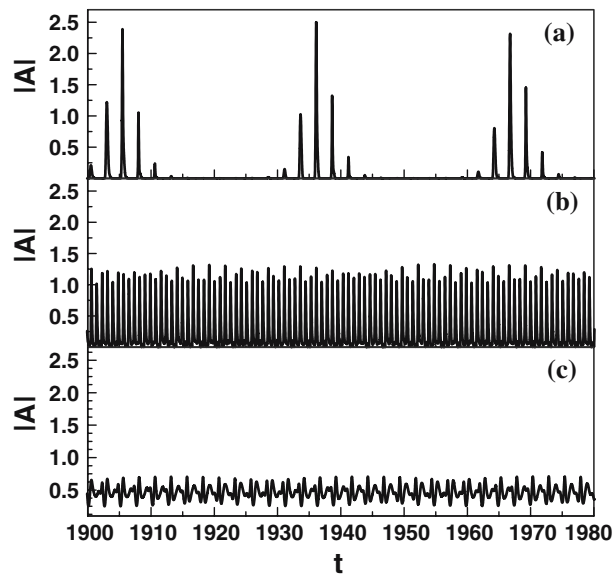


Fig. 12. Intensity timetraces of Equations (9)–(11) illustrating irregular pulsating regimes. $q_0 = 2$, (a) Q-switching ML regime, $g_0 = 0.3$; (b) irregular pulsing, $g_0 = 1.75$; (c) $g_0 = 2.0$. Other parameters are the same as in Fig. 9.

been integrated from $t = 0$ to $t = 20$ ns in order to skip transient behavior. Next, during a time interval $\Delta t = 5$ ns local maxima and minima of the time dependence of the laser intensity $|A|$ for each given value of the unsaturated gain parameter g_0 have been plotted. It follows from Fig. 10 that at small g_0 the laser exhibits a regime of Q-switched ML. This regime is characterized by a sequence of ML pulses with the pulse peak power strongly modulated with the Q-switching frequency. The corresponding intensity time trace is presented in Fig. 12(a). With the increase of g_0 this supermodulation disappears and a regime of pure fundamental ML becomes stable (see time trace in Fig. 11(a)). When the unsaturated gain parameter is further increased transitions to ML regimes with higher repetition rates take place. The regimes with the pulse repetition rate approximately equal 80 and 120 GHz are shown in Fig. 11(b) and (c), respectively. The stability ranges of the harmonic ML regimes are smaller than those of the fundamental ML regime and decrease with increasing repetition frequency. Thus the greater the repetition frequency of a harmonic ML regime the harder is its experimental observation. According to Fig. 10 the ML behavior breaks up with the appearance of irregular oscillations of the pulse peak power (see time traces in Fig. 12(b) and (c)) and finally at large values of g_0 a transition to a CW operation occurs. The bifurcation sequence shown in Fig. 10 is in qualitative agreement with the results of numerical simulations of the TWE model as well as with experimental data.

5. Conclusion

We have studied both theoretically and experimentally typical operation regimes of 40 GHz monolithic mode-locked lasers. Thereby, we demonstrated the validity of the underlying TWE model, the results of which agree very well with the measurements. Simulations with the TWE model revealed quantitative agreement for characteristics of ML as pulse width and frequency tuning, as well as qualitative agreement in location and behaviour of other dynamic scenaria. Furthermore, the appearance of stable harmonic ML at 80 GHz has been predicted by the TWE model and found later by measurements in the same parameter region. Having twice higher repetition rate in comparison with the fundamental ML regime, this regime is characterized by larger pulse width, as it follows from Figs. 3, 4, 7, and 11. Moreover, we have analyzed a related DDE-model which guided us to a qualitative understanding of the observed phenomena. The DDE model especially confirms our findings on harmonic ML at 80 GHz and predicts even higher harmonics of ML. According to this model 80 GHz harmonic ML appears after the leading edge instability of the fundamental ML regime.

Acknowledgement

The authors acknowledge the financial support by the project TerabitOptics Berlin, Grant B1-1911, and by the DFG-research center MATHEON.

Notes

1. SIPBH: semi-insulating planar buried heterostructure.
2. Local power at z divided by the constant $\hbar\omega_0 v_g \sigma$, v_g : group velocity, σ : cross section area of the active zone.
3. A possible detuning via the refractive index is not considered here.

References

- Avrutin, E., V. Nikolaev and D. Gallagher. *Optoelectronic Devices: Advanced Simulation and Analysis*, chapter 7: Monolithic Mode-Locked Semiconductor Lasers, p. 185–215. J. Piprek, 2005.
- Bandelow, U., M. Radziunas, J. Sieber and M. Wolfrum. *IEEE J. Quantum Electron.* **37**(2) 183–188, 2001.
- Bandelow, U., H. Wenzel and H.-J. Wünsche. *Electron. Lett.* **28** 1324–1326, 1992.
- Engelborghs, K., T. Luzyanina and G. Samaey. DDE-BIFTOOL v. 2.00: A matlab package for bifurcation analysis of delay differential equations. Technical Report TW-330, Department of Computer Science, K.U. Leuven, Leuven, Belgium, 2001.
- Guglielmi, N. and E. Hairer. *Users' Guide for the Code RADAR5*, 2000.
- Haus, H. *IEEE J. Sel. Top. Quantum Electron.* **6** 1173–1185, 2001.
- Kaiser, R., B. Hüttl, H. Heidrich, S. Fidorra, W. Rehbein, H. Stolpe, R. Stenzel, W. Ebert and G. Sahin. *IEEE Photon. Technol. Lett.* **15**(5) 634–636, 2003.
- New, G.H.C. *IEEE J. Quantum Electron.* **10** 115–124, 1974.
- Rachinskii, D. and A. Vladimirov. Q-switching instability in a mode-locked semiconductor laser. WIAS preprint 975, 2004.
- Radziunas, M., H.-J. Wünsche, B. Sartorius, O. Brox, D. Hoffmann, K. Schneider and D. Marcenac. *Optoelectronic Devices: Advanced Simulation and Analysis*, chapter 5: Multisection Lasers: Longitudinal Modes and their Dynamics, pp. 121–150. J. Piprek, 2005.
- Vladimirov, A., D. Turaev and G. Kozyreff. *Opt. Lett.* **29** 1221–1223, 2004.
- Wünsche, H.-J., M. Radziunas, S. Bauer, O. Brox and B. Sartorius. *IEEE J. Selected Topics Quantum Electron.* **9**(3) 857–864, 2003.